Amino Acids (2021) 53:517–532
https://doi.org/10.1007/s00726-020-02911-7

ORIGINAL ARTICLE

Monitoring peptide tyrosine nitration by spectroscopic methods

Petr Niederhafner[1,2] · Martin Šafařík[1] · Jitka Neburková[1] · Timothy A. Keiderling[3] · Petr Bouř[1] · Jaroslav Šebestík[1]

Received: 25 August 2020 / Accepted: 4 November 2020 / Published online: 18 November 2020

Abstract

Oxidative stress can lead to various derivatives of the tyrosine residue in peptides and proteins. A typical product is 3-nitro-L-tyrosine residue (Nit), which can affect protein behavior during neurodegenerative processes, such as those associated with Alzheimer's and Parkinson's diseases. Surface enhanced Raman spectroscopy (SERS) is a technique with potential for detecting peptides and their metabolic products at very low concentrations. To explore the applicability to Nit, we use SERS to monitor tyrosine nitration in Met-Enkephalin, rev-Prion protein, and α-synuclein models. Useful nitration indicators were the intensity ratio of two tyrosine marker bands at 825 and 870 cm^{-1} and a bending vibration of the nitro group. During the SERS measurement, a conversion of nitrotyrosine to azobenzene containing peptides was observed. The interpretation of the spectra has been based on density functional theory (DFT) simulations. The CAM-B3LYP and ωB97XD functionals were found to be most suitable for modeling the measured data. The secondary structure of the α-synuclein models was monitored by electronic and vibrational circular dichroism (ECD and VCD) spectroscopies and modeled by molecular dynamics (MD) simulations. The results suggest that the nitration in these peptides has a limited effect on the secondary structure, but may trigger their aggregation.

Keywords Nitration · Oxidative stress · Surface-enhanced Raman spectroscopy (SERS) · Vibrational circular dichroism (VCD) · Electronic circular dichroism (ECD) · Density functional theory (DFT)

Abbreviations

ACN	Acetonitrile
Bn	Benzyl
CCT	Cartesian coordinate-based tensor transfer method
CPCM	Conductor-like polarizable continuum model
DFT	Density functional theory
DIC	*N,N′*-Diisopropylcarbodiimide
DMF	*N,N*-Dimethylmethanamide
ECD	Electronic circular dichroism
EDT	1,2-Ethanedithiol
ESI	Electrospray ionization
Fmoc	9-Fluorenylmethoxycarbonyl
FWHH	Full width (of a spectral peak) at half height
GSH	Glutathione
HF	Hartree Fock
HOBt	*N*-Hydroxybenzotriazole
HPLC	High-performance liquid chromatography
IR	Infrared absorption
MALDI	Matrix-assisted laser desorption/ionization
MS	Mass spectrometry
Nit	3-Nitro-*L*-tyrosine
PDB id.	Four letter identification code of a structure deposited in the RCSB Protein Data Bank
PTM	Posttranslational modification
ROA	Raman optical activity
SERS	Surface-enhanced Raman spectroscopy
tBu	*tert*-Butyl
TEM	Transmission electron microscopy
TFA	Trifluoroacetic acid

Handling editor: D. Tsikas.

Electronic supplementary material The online version of this article (https://doi.org/10.1007/s00726-020-02911-7) contains supplementary material, which is available to authorized users.

✉ Jaroslav Šebestík
sebestik@uochb.cas.cz

[1] Institute of Organic Chemistry and Biochemistry, Academy of Sciences, Flemingovo náměstí 2, 16610 Prague 6, Czech Republic

[2] Department of Chemistry of Natural Compounds, Faculty of Food and Biochemical Technology, University of Chemistry and Technology, Prague, Technická 5, 166 28 Prague 6, Czech Republic

[3] Department of Chemistry, University of Illinois at Chicago, 845 W. Taylor St., Chicago, IL 60607-7061, USA

TOF	Time of flight (detection)
TIS	Triisopropyl silane
VCD	Vibrational circular dichroism

Introduction

During oxidative stress in living cells, reactive oxygen and nitrogen species are generated (Beckman et al. 1990; Beckman and Crow 1993; Ježek et al. 2017). These radicals can cause either direct nitration of tyrosine or covalent crosslinking of two tyrosines leading to protein oligomerization (Radi 2004, 2013; Reynolds et al. 2005; Vana et al. 2011). For simplification, in this paper the nitration will exclusively refer to processes leading to formation of 3-nitro-L-tyrosine (Nit). For example, protein plaques in the brains of patients with various synucleinopathies contained nitrated α-synuclein (Duda et al. 2000; Giasson et al. 2000). The α-synuclein oligomerization is a very complex process (Gurry et al. 2013) and tyrosine nitration can further alter its pathways: Lashuel and co-workers showed how site-specific nitration at either tyrosine 39 or 125 influenced α-synuclein structure and led to amorphous aggregates (Burai et al. 2015). The nitration also inhibited interactions between α-synuclein and membranes. Thus, studying α-synuclein nitration and its influence on protein properties can be important for understanding the neurodegenerative processes.

Monitoring of posttranslational modifications (PTM) of proteins is crucial for understanding processes that govern cellular division, growth, differentiation, recognition, and regulation of metabolism. The term PTM is used for changes in the peptide covalent structure as a result of chemical or enzymatic reaction (Larsen et al. 2006). 3-Nitro-L-tyrosine (Nit) formation belongs to one of the very important PTM of proteins (Abello et al. 2009; Castro et al. 2011; Aslan and Dogan 2011; Yttenberg and Jensen 2010; Campolo et al. 2020).

Tandem mass spectrometry in combination with either gas chromatography (GC–MS, GC–MS/MS) or liquid chromatography (LC–MS/MS) has been frequently used for qualitative and quantitative analyses of free and proteinic 3-nitro-L-tyrosine in biological samples (Larsen et al. 2006; Tsikas and Duncan 2014).

Nitration of tyrosine and of some proteins has previously been investigated using Raman spectroscopy. Namely characterization of 3-nitro-L-tyrosine (Izzo et al. 1982), and nitrated proteins such as hen egg lysozyme (Izzo et al. 1982), superoxide dismutase (Ischiropoulos et al. 1992), cytochrome c (Quaroni and Smith 1999a) and human iron regulatory protein 1 (Soum et al. 2003) were reported. Two-dimensional infrared spectroscopy is another technique previously used for detection and quantification of 3-nitrotyrosine (Valim et al. 2014).

UV–Vis and electronic circular dichroism (ECD) spectroscopies of an enzyme and of a model diketopiperazine containing 3-nitrotyrosine have also been reported (Di Bello and Griffin 1975). ECD spectroscopy provided information on nitration of human islet amyloid polypeptide (Zhao et al. 2019). However, due to the strong interfering contributions of the aromatic chromophore, interpretation of the experimental ECD spectra in terms of secondary structure without theoretical calculations was not conclusive (Woody and Woody 2003; Hudecová et al. 2012).

Due to their higher resolution in comparison with the electronic methods, IR and vibrational circular dichroism (VCD) can provide more detailed information about protein secondary structure than UV–Vis and ECD (Kessler et al. 2018; Keiderling 2020). This is possible also for analyses of Raman optical activity (ROA) (Barron et al. 2000, 2004, 2006; Barron and Buckingham 2010; Barron 2012). However, VCD and ROA measurements require relatively high concentrations of studied substrates, which are often not possible, particularly under physiological conditions.

On the other hand, surface-enhanced Raman spectroscopy (SERS) can detect peptides at concentrations down to sub mM levels (Seballos et al. 2007; Kurouski et al. 2017). SERS can be achieved on various platforms, such as nanoparticle and substrate based systems (Kurouski et al. 2017; Guerrini and Graham 2012). Different nanoparticles provide different enhancement factors (Zhang et al. 2014a, b; Betz et al. 2014; Kleinman et al. 2013; Sharma et al. 2012). Nanoparticles of various porosities and shapes, including sharp-edges in star-like structures, have been employed (Mulvihill et al. 2010; Rycenga et al. 2012; Shao et al. 2013; Jing et al. 2014; Zhang et al. 2014a, b). A drawback of SERS studies with nanoparticles can be interference by strong signals from nanoparticle stabilizers, such as citrate and cetyltrimethylammonium bromide (Kurouski and van Duyne 2015; Martinsson et al. 2015), which are necessary for their stabilization. Leopold and Lendl (2003) prepared "surfactant free" nanoparticles with controlled size and dispersion. Various strategies for nanoparticle assembly were also described, based on electrostatic modulation or functionalization of the colloid surface with DNA or small organic molecules (Graham et al. 2008; Taylor et al. 2011; Alvarez-Puebla et al. 2009). In the present study, we developed a protocol based on silver nanoparticles stabilized by citrate.

To explore the possibilities of SERS for analysis of the nitrated tyrosine products, we have investigated peptide models derived from α-synuclein with all possible permutations of tyrosine and nitrotyrosine in the sequences, i.e. specifically for the αSyn25-53 and αSyn118-140 peptide series (Fig. 1), whose synthesis has been described in refs. (Niederhafner et al. 2016) and (Niederhafner et al. 2019a). Their secondary structures in solution were monitored using a combination of the chiroptical spectroscopies and theoretical

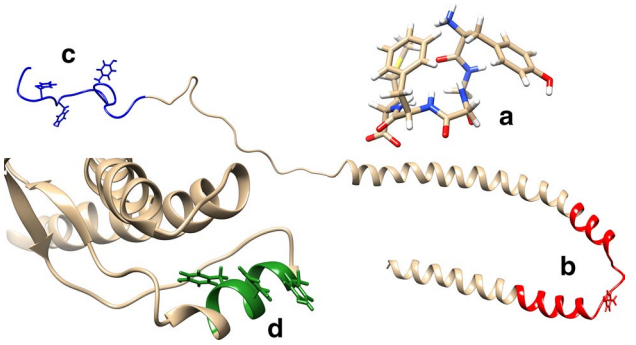

Fig. 1 Model peptides and their protein sources selected for SERS: **a** Met-enkephalin (PDB id. 2LWC)—endogenous opioid peptide (Krajnik et al. 2010), **b** α-synuclein (PDB id. 1XQ8, Ulmer et al. 2005)—red αSyn25-53—a domain abundant for pathological mutations and also for pathological nitration (Burai et al. 2015; Meade et al. 2019), **c** α-synuclein (PDB id. 1XQ8)—blue αSyn118-140 domain involved in phosphorylation and Lewy body formation (Fujiwara et al. 2002; Oueslati et al. 2010; Anderson et al. 2006; Meade et al. 2019), and **d** Human prion protein (PDB id. 1QM2, Zahn et al. 2000)—green HuPrP145-151—belonging to sequence recognized by NCAM transmembrane proteins (Martins et al. 2010). Images were visualized using program Chimera (Pettersen et al. 2004)

calculations. We have found a reproducible SERS protocol for detection of nitrotyrosine in synuclein, Met-enkephalin and prion protein related peptides, which also provide cheap and easily accessed substrates for further development of the spectroscopic techniques.

Experimental part

Peptide synthesis

The αSyn118-140 and αSyn25-53 peptide series were synthesized by the Fmoc/tBu method (Fields and Noble 1990) on an automatic solid-phase synthesizer ABI 433A (Applied Biosystems) using the FastMoc 0.1 mmol program (SynthAssist™ version 3.1) with a single coupling: 10 eq of an excess of protected amino acids and HBTU coupling reagent and 20 eq of an excess of DIPEA were used. Nitrotyrosine containing peptides were prepared using Fmoc-Nit(Bn)-OH (Niederhafner et al. 2016, 2019a), thus, the peptides were obtained with a defined sequence containing solely Nit at selected positions without contamination with 3,3′-dityrosine. The peptides were cleaved from the resin by mixture of TFA (4.5 mL), H_2O (150 µL), EDT (150 µL), thioanisole (150 µL), and TIS (50 µL) for 4 h, unless stated otherwise. Other peptides were synthesized with the Fmoc/tBu method (Fields and Noble 1990) by manual solid-phase synthesis using a quadruple molar excess of Fmoc-protected amino acids (0.21 mmol) and coupling reagents DIC (33 µL; 0.21 mmol) and HOBt (28 mg; 0.21 mmol) in DMF (2 mL). Peptide deprotection was done within the cleavage from the resin. All the peptides were prepared in more than 95% purity (HPLC chromatograms and MS data are available in Supplementary information).

Chromatographic and MS methods

During the syntheses, molecular weights of peptide fragments were determined using a matrix assisted laser desorption ionization and electrospray ionization mass spectroscopies (MALDI-TOF and ESI, respectively). For HPLC, an instrument with a quaternary pump, thermostat, diode array detector and reverse-phase C_{18} columns was used. The peptides were purified by semipreparative HPLC on the VYDAC 250 × 10 mm, 10 µm RP-18 column with a flow rate 3 mL/min using a 0–100% ACN (acetonitrile) gradient in 0.05% aqueous TFA. Analytical HPLC was carried out with a Poroshell 120 SB-C18 2.7 mm, 3.0 × 50 mm column, a flow rate 1 mL/min, and diode array detection using method A with gradient 5–50% of ACN in 0.05% aqueous TFA within 0–10 min or method B with gradient 5–5–100% of ACN in 0.05% aqueous TFA within 0–1–10 min.

Fmoc-Nit(Bn)-OH – *O*-Benzyl-*N*-(9-fluorenylmethoxycarbonyl)-3-nitro-L-tyrosine – (1)

We have combined and improved on the procedures for syntheses of H-Tyr(Bn)-OH (Bodanszky and Bodanszky 1994), H-Tyr[Bn(2,6-Cl_2)]-OH (Erickson and Merrifield 1973; Yamashiro and Li 1973), and Fmoc-Nit(Bn)-OH (Niederhafner et al. 2016; Niederhafner et al. 2019a, b). To commercially available H-Nit-OH (5.3 g, 23.4 mmol) in 2 M NaOH (23.3 mL, 46.6 mmol), a solution of $CuSO_4.5H_2O$ (2.9 g in 17 mL H_2O, 11.6 mmol) was added. The mixture was shortly heated to 60 °C, then it was cooled to rt, diluted with MeOH (100 mL) and made more alkaline by addition of 2 M NaOH (3.5 mL, 7.0 mmol). Then benzyl bromide (2.75 mL, 22.7 mmol) was added and the mixture was vigorously stirred at rt. After 1 h, a second portion of benzyl bromide (2.75 mL, 22.7 mmol) was added and the mixture was stirred at rt overnight. In order to avoid separation problems caused by incomplete reaction, the conversion was monitored: the sample (50 µL) of reaction mixture was suspended in EtOH:water (1:1) mixture (200 µL) and Chelaton III (5 mg) was added. After 5 min sonication, the solution was analyzed by TLC using ACN: 25% NH_4OH (7:1) mobile phase. Unreacted H-Nit-OH and intermediate H-Nit(Bn)-OH had R_F 0.43 and 0.60, respectively. If the starting material was observed, another portion of benzyl bromide (2.75 mL, 22.7 mmol) was added and the reaction continued for 4 h. After completion, the blue-green oil was covered by *n*-hexane and left standing to crystallize for 16 h. The suspension was filtered

off, blue solid was collected, and washed with *n*-hexane (3 × 300 mL) and dried under vacuum for 2 h. The complex [Cu(H-Nit(Bn)-O)$_2$] (10.4 g, 15 mmol) was dissolved in water/dioxane (120 mL) with Chelaton III (15.0 g, 40.3 mmol) and stirred on an ice bath for 10 min. Subsequently, 450 mL acetone and Fmoc-OSu (2.8 g, 8.3 mmol) were added to the reaction mixture. pH was maintained at 9.2 by 10% aqueous Na_2CO_3 for 6 h at room temperature. The suspension was washed with ether (2 × 100 mL). The aqueous layer was acidified with aqueous $KHSO_4$ to pH 3. The aqueous solution was extracted with ethyl acetate (3 × 250 mL). The combined organic layers were collected and dried over anhydrous Na_2SO_4. Solvent was removed in vacuum, the product was obtained as a yellow crystals Fmoc-Nit(Bn)-OH. Yield 2.9 g (65% based on Fmoc-OSu). HPLC: R_T 7.5 min (B). For $C_{31}H_{26}N_2O_7$ (538.17), found ESI–MS *m/z*: 561.3 ([M + Na]$^+$); 577.3 ([M + K]$^+$). **Rf** (EtOAc–CH3OH 16:1) 0.25 (0.24 lit. (Niederhafner et al. 2016)). **Mp** 105–108 °C (103–105 °C lit. (Niederhafner et al. 2016)). **^{1}H-NMR** (400 MHz, DMSO-*d6*) δ 7.87 (d, *J* = 7.5 Hz, 2H, $H4_{Fmoc}$), 7.84 (d, *J* = 2.1 Hz, 1H, $H2_{Nit}$), 7.78 (d, *J* = 8.6 Hz, 1H, NH), 7.62 (d, *J* = 7.5 Hz, 2H, $H1_{Fmoc}$), 7.55 (dd, J = 8.7, 2.1 Hz, 1H, $H6_{Nit}$), 7.47–7.24 (m, 10H, $H2_{Fmoc}$ + H2–4_{Bn} + $H3_{Fmoc}$ + $H5_{Nit}$), 5.24 (s, 2H, $CH_{2,Bn}$), 4.18 (m, 4H, $CH\alpha_{Nit}$ + CH_{2Fm} + $H9_{Fmoc}$), 3.12 (dd, J = 13.9, 4.3 Hz, 1H, $CH\beta_{Nit}$), 2.88 (dd, *J* = 13.8, 10.9 Hz, 1H, $CH\beta_{Nit}$). **^{13}C-NMR** (100 MHz, DMSO-*d6*) δ 172.99 ($COOH_{Nit}$), 155.98 ($NHCOO_{Fmoc}$), 149.67 ($C4_{Nit}$), 143.73 ($C9a_{Fmoc}$), 140.69 ($C4a_{Fmoc}$), 139.16 ($C3_{Nit}$), 136.04 ($C1_{Bn}$), 135.14 ($C6_{Nit}$), 130.77 ($C1_{Nit}$), 128.52 ($C3_{Bn}$), 128.06 ($C4_{Bn}$), 127.63 ($C2_{Fmoc}$), 127.38 ($C2_{Bn}$), 127.04 ($C3_{Fmoc}$), 125.55 ($C2_{Nit}$), 125.19 ($C1_{Fmoc}$), 120.11 ($C4_{Fmoc}$), 115.32 ($C5_{Nit}$), 70.41 ($CH_{2,Bn}$), 65.69 (CH_{2Fmoc}), 55.14 ($CH\alpha_{Nit}$), 45.55 ($H9_{Fmoc}$), 34.98($CH\beta_{Nit}$).

Met-enkephalin

H-Tyr-Gly-Gly-Phe-Met-OH (**2**) – HPLC: R_T 2.7 min (A). When the B method was used, the compound appeared in the inject peak (0.3 min) i.e. without significant retention by the column. For $C_{27}H_{35}N_5O_7S$ (573.23), found ESI–MS *m/z*: 574.3 ([M + H]$^+$); 596.3 ([M + Na]$^+$); 612.2 ([M + K]$^+$). Amino acid analysis: Tyr 1.15 (1), Gly 2.30 (2), Phe 1.00 (1), Met 0.96 (1).

[Nit^1]Met-enkephalin

H-Nit-Gly-Gly-Phe-Met-OH (**3**) – HPLC: R_T 4.2 min (B). For $C_{27}H_{34}N_6O_9S$ (618.21) found ESI–MS, *m/z*: 619.4 ([M + H]$^+$); 641.4 ([M + Na]$^+$). Amino acid analysis: Nit 0.73 (1), Gly 2.24 (2), Phe 1.02 (1), Met 1.00 (1).

rev-Prion protein (145–151) – revHuPrP145-151

H-Arg-Tyr-Tyr-Arg-Asp-Glu-Tyr-OH (**4**) – HPLC: R_T 2.9 min (B). For $C_{48}H_{65}N_{13}O_{15}$ (1063.47) found ESI–MS, *m/z*: 1064.6 ([M + H]$^+$); 1086.5 ([M + Na]$^+$). Amino acid analysis: Arg 1.76 (2), Tyr 3.00 (3), Asp 1.00 (1), Glu 1.08 (1).

[Nit^{150}]rev-Prion protein (145–151) – rev[Nit^{150}] HuPrP145-151

H-Arg-Nit-Tyr-Arg-Asp-Glu-Tyr-OH (**5**) – HPLC: R_T 3.26 min (B). For $C_{48}H_{64}N_{14}O_{17}$ (1108.46) found ESI–MS, *m/z*: 1109.5 ([M + H]$^+$); 1131.5 ([M + Na]$^+$). Amino acid analysis: Arg 1.96 (2), Tyr 2.27 (2), Asp 1.06 (1), Glu 1.16 (1), Nit 1.00 (1).

[Nit^{149}]rev-Prion protein (145–151) – rev[Nit^{149}] HuPrP145-151

H-Arg-Tyr-Nit-Arg-Asp-Glu-Tyr-OH (**6**) – HPLC: R_T 3.3 min (B). For $C_{48}H_{64}N_{14}O_{17}$ (1108.46) found ESI–MS, *m/z*: 1109.5 ([M + H]$^+$); 1131.5 ([M + Na]$^+$). Amino acid analysis: Arg 1.85 (2), Tyr 2.20 (2), Asp 0.97 (1), Glu 1.00 (1), Nit 0.88 (1).

[Nit^{145}]rev-Prion protein (145–151) – rev[Nit^{145}] HuPrP145-151

H-Arg-Tyr-Tyr-Arg-Asp-Glu-Nit-OH (**7**) – HPLC: R_T 3.4 min (B). For $C_{48}H_{64}N_{14}O_{17}$ (1108.46) found ESI–MS, *m/z*: 1109.6 ([M + H]$^+$); 1131.6 ([M + Na]$^+$). Amino acid analysis: Arg 2.14 (2), Tyr 1.80 (2), Asp 0.97 (1), Glu 1.07 (1), Nit 1.00 (1).

αSyn25-53

H-Gly-Val-Ala-Glu-Ala-Ala-Gly-Lys-Thr-Lys-Glu-Gly-Val-Leu-Tyr-Val-Gly-Ser-Lys-Thr-Lys-Glu-Gly-Val-Val-His-Gly-Val-Ala-OH (**8**) – HPLC: R_T 3.2 min (B). For $C_{125}H_{209}N_{35}O_{40}$ (2840.54) found MALDI-MS, *m/z*: 2841.6 ([M + H]$^+$); 2864.6 ([M + Na + H]$^+$); 2881.6 ([M + K + H]$^+$). Amino acid analysis: Ala 4.11 (4), Glu 3.50 (3), Gly 6.00 (6), Tyr 1.20 (1), Thr 1.88 (2), Ser 0.94 (1), His 1.73 (1), Lys 4.26 (4), Leu 1.12 (1), Val 5.27 (6).

[Nit^{39}]αSyn25-53

H-Gly-Val-Ala-Glu-Ala-Ala-Gly-Lys-Thr-Lys-Glu-Gly-Val-Leu-Nit-Val-Gly-Ser-Lys-Thr-Lys-Glu-Gly-Val-Val-His-Gly-Val-Ala-OH (**9**) – HPLC: R_T 4.5 min (B). For $C_{125}H_{208}N_{36}O_{42}$ (2885.52) found MALDI-MS, *m/z*: 2887.4 ([M + 2H]$^+$); 2909.4 ([M + Na + H]$^+$); 2925.4 ([M + K] +).

Amino acid analysis: Ala 4.02 (4), Glu 3.50 (3), Gly 6.00 (6), Thr 1.94 (2), Ser 0.90 (1), His 1.10 (1), Lys 4.03 (4), Leu 1.12 (1), Val 5.21 (6), Nit 0.84 (1).

αSyn118-140

H-Val-Asp-Pro-Asp-Asn-Glu-Ala-Tyr-Glu-Met-Pro-Ser-Glu-Glu-Gly-Tyr-Gln-Asp-Tyr-Glu-Pro-Glu-Ala-OH (**10**) – HPLC: R_T 3.3 min (B). For $C_{114}H_{157}N_{25}O_{48}S$ (2676.03) found MALDI-MS, *m/z*: 2682.0 ($[M+4H]^+$), 2700.0 ($[M+H+Na]^+$); 2716.0 ($[M+H+K]^+$), 2739.0 ($[M+H+Na+K]^+$). Amino acid analysis: Ala 2.00 (2), Asp + Asn 3.62 (4), Glu + Gln 7.34 (7), Gly 0.98 (1), Pro 3.22 (3), Tyr 3.14 (3), Ser 0.78 (1), Met 0.82 (1), Val 0.87 (1).

[Nit^{125}]αSyn118-140

H-Val-Asp-Pro-Asp-Asn-Glu-Ala-Nit-Glu-Met-Pro-Ser-Glu-Glu-Gly-Tyr-Gln-Asp-Tyr-Glu-Pro-Glu-Ala-OH (**11**) – HPLC: R_T 4.0 min (B). For $C_{114}H_{156}N_{26}O_{50}S$ (2721.02) found MALDI-MS, *m/z*: 2745.1 ($[M+H+Na]^+$), 2761.1 ($[M+K]^+$). Amino acid analysis: Ala 1.88 (2), Asp + Asn 3.74 (4), Glu + Gln 7.32 (7), Gly 1.00 (1), Pro 2.67 (3), Tyr 2.04 (2), Ser 0.80 (1), Met 0.76 (1), Val 0.90 (1), Nit 0.91 (1).

[Nit^{133}]αSyn118-140

H-Val-Asp-Pro-Asp-Asn-Glu-Ala-Tyr-Glu-Met-Pro-Ser-Glu-Glu-Gly-Nit-Gln-Asp-Tyr-Glu-Pro-Glu-Ala-OH (**12**) – HPLC: R_T 3.3 min (B). For $C_{114}H_{156}N_{26}O_{50}S$ (2721.02) found MALDI-MS, *m/z*: 2744.9 ($[M+H+Na]^+$); 2760.9 ($[M+K]^+$). Amino acid analysis: Ala 1.88 (2), Asp + Asn 3.68 (4), Glu + Gln 7.24 (7), Gly 1.00 (1), Pro 2.85 (3), Tyr 2.01 (2), Ser 0.78 (1), Met 0.78 (1), Val 0.82 (1), Nit 0.94 (1).

[Nit^{136}]αSyn118-140

H-Val-Asp-Pro-Asp-Asn-Glu-Ala-Tyr-Glu-Met-Pro-Ser-Glu-Glu-Gly-Tyr-Gln-Asp-Nit-Glu-Pro-Glu-Ala-OH (**13**) – HPLC: R_T 3.5 min (B). For $C_{114}H_{156}N_{26}O_{50}S$ (2721.02) found MALDI-MS, *m/z*: 2745.0 ($[M+H+Na]^+$), 2761.0 ($[M+K]^+$). Amino acid analysis: Ala 2.03 (2), Asp + Asn 3.78 (4), Glu + Gln 7.26 (7), Gly 1.07 (1), Pro 3.11 (3), Tyr 2.18 (2), Ser 0.86 (1), Met 0.85 (1), Val 0.88 (1), Nit 1.00 (1).

[Nit^{125,133}]αSyn118-140

H-Val-Asp-Pro-Asp-Asn-Glu-Ala-Nit-Glu-Met-Pro-Ser-Glu-Glu-Gly-Nit-Gln-Asp-Tyr-Glu-Pro-Glu-Ala-OH (**14**) – HPLC: R_T 4.2 min (B). For $C_{114}H_{155}N_{27}O_{52}S$ (2766.00) found MALDI-MS, *m/z*: 2790.1 ($[M+H+Na]^+$); 2806.1 ($[M+K]^+$). Amino acid analysis: Ala 1.91 (2), Asp 3.79 (4), Glu 7.54 (7), Gly 0.94 (1), Pro 3.01 (3), Tyr 1.00 (1), Ser 0.79 (1), Met 0.84 (1), Val 0.85 (1), Nit 1.62 (2).

[Nit^{125,136}]αSyn118-140

H-Val-Asp-Pro-Asp-Asn-Glu-Ala-Nit-Glu-Met-Pro-Ser-Glu-Glu-Gly-Tyr-Gln-Asp-Nit-Glu-Pro-Glu-Ala-OH (**15**) – The peptide was cleaved from the resin by mixture of TFA (4.5 mL), H_2O (150 µL), EDT (150 µL), thioanisole (150 µL), and TIS (50 µL) for 8 h HPLC: R_T 4.2 min (B). For $C_{114}H_{155}N_{27}O_{52}S$ (2766.00) found MALDI-MS, *m/z*: 2790.1 ($[M+H+Na]^+$); 2806.1 ($[M+K]^+$). Amino acid analysis: Ala 2.00 (2), Asp 4.02 (4), Glu 7.86 (7), Gly 1.01 (1), Pro 3.62 (3), Tyr 1.13 (1), Ser 0.89 (1), Met 0.72 (1), Val 0.94 (1), Nit 1.61 (2).

[Nit^{133,136}]αSyn118-140

H-Val-Asp-Pro-Asp-Asn-Glu-Ala-Tyr-Glu-Met-Pro-Ser-Glu-Glu-Gly-Nit-Gln-Asp-Nit-Glu-Pro-Glu-Ala-OH (**16**) – HPLC: R_T 4.2 min (B). For $C_{114}H_{155}N_{27}O_{52}S$ (2766.00) found MALDI-MS, *m/z*: 2790.1 ($[M+H+Na]^+$); 2806.0 ($[M+K]^+$). Amino acid analysis: Ala 1.96 (2), Asp + Asn 3.73 (4), Glu + Gln 7.23 (7), Gly 1.01 (1), Pro 3.10 (3), Tyr 1.03 (1), Ser 0.80 (1), Met 0.79 (1), Val 1.00 (1), Nit 1.79 (2).

[Nit^{125,133,136}]αSyn118-140

H-Val-Asp-Pro-Asp-Asn-Glu-Ala-Nit-Glu-Met-Pro-Ser-Glu-Glu-Gly-Nit-Gln-Asp-Nit-Glu-Pro-Glu-Ala-OH (**17**) – HPLC: R_T 4.3 min (B). For $C_{114}H_{154}N_{28}O_{54}S$ (2810.99) found MALDI-MS, *m/z*: 2835.1 ($[M+H+Na]^+$); 2855.2 ($[M+2Na]^+$). Amino acid analysis: Ala 1.91 (2), Asp 3.78 (4), Glu 7.46 (7), Gly 1.00 (1), Pro 3.03 (3), Ser 0.82 (1), Met 0.77 (1), Val 0.82 (1), Nit 2.73 (3).

Preparation of silver nanoparticles

Borate nanoparticles (18)

Borate stabilized silver nanoparticles were prepared according to Mulfinger et al. (2007). The solution was stored at 5 °C. UV–Vis: $\lambda_{max} = 397$ nm, full width at half height (FWHH) was 60 nm.

Citrate nanoparticles (19)

Citrate silver nanoparticles were grown according to Stamplecoskie et al. (2011). Borate stabilized particles (**18**), aged

at least one day and no older than one month, served as seeds. 3 mL of solution A (0.2 mM $AgNO_3$ and 1.0 mM trisodium citrate) were well mixed with various amounts of seed solution (**18**): 125, 250, 375, or 500 µL. Then, 1 mL of 10 mM ascorbic acid solution was added dropwise during gentle shaking for 3 min. Note that the reproducibility of colloid preparation depends on mixing of the Ag(I) solution with ascorbic acid. Obtained solutions exhibited these UV–Vis parameters: **19a**: λ_{max} 410 nm (FWHH 110 nm), 572 nm (FWHH 264 nm), **19b**: λ_{max} 471 nm (FWHH 211 nm), **19c**: λ_{max} 449 nm (FWHH 163 nm), and **19d**: λ_{max} 415 nm (FWHH 78 nm), see Figures S1 and S2. The solutions were left for several days to mature (at least 72 h at room temperature) and then stored in darkness at 5 °C for several months. Unless stated otherwise, **19c** was used for SERS measurement by default.

Transmission electron microscopy (TEM)

Carbon-coated copper grids were placed into a UV-ozonizing chamber (UV/Ozone Pro Cleaner Plus, Bioforce Nanosciences) for 15 min as described by Rehor and Cigler (2014). Then a droplet of poly(ethyleneimine) (2.5 kDa, 0.1 mg/mL) was deposited on the grid and removed after 10 min incubation using a piece of tissue. Similarly, a droplet of aqueous solution of silver sol was deposited on the grid and removed after 3 min. TEM images were captured using a JEOL JEM-1011 electron microscope operated at 80 kV.

Raman and SERS spectra

Raman spectra acquired with a BioTools ChiralRAMAN-2X instrument (532 nm excitation wavelength, 1.03–2.06 s illumination time per scan) were processed using home-made software (Šebestík and Bouř 2011; Šebestík et al. 2012). SERS has been used to detect protein nitration in Met-enkephalin (pentapeptide), mono-nitration of reverse human prion peptide 145–151 (4 × heptapeptides), all permutations of Tyr and Nit in αSyn118-140 (8 × 23-peptides), and αSyn25-53 (2 × 29-peptide) by loading the peptides on silver nanoparticles. For SERS measurement (Seballos et al. 2007), 1 M HCl was added for suppression of colloidal background and the spectra were obtained for mixtures of Ag sol (60 µL, **18** or **19a-d**), a 10^{-4} M sample solution (10 µL), and 1 M HCl (10 µL) with 1.40 s illumination time per scan.

ECD spectra

ECD spectra for αSyn118-140 and αSyn25-53 peptide series were measured using a Jasco J-810 spectrometer. The samples were held in 0.1 cm path length quartz cells, using concentrations of about 0.2 mg mL^{-1} in water. Each spectrum was obtained as average of six scans taken with a band pass of 1 nm and scanning speed of 50 nm/min.

IR and VCD spectra

VCD spectra of αSyn118-140 and αSyn25-53 peptide series were measured using a custom-made dispersive instrument separately described elsewhere (Lakhani et al. 2009; Keiderling and Lakhani 2018). IR spectra were recorded using a Vertex 80 FTIR (Bruker) spectrometer. After 6 cycles of hydrogen chloride saturation (dissolution in 1 mL of 5 mM HCl and evaporation to dryness) and 3 cycles of deuterium exchange (dissolution in 1 mL D_2O with subsequent freeze drying), the samples were prepared by dissolving the exchanged peptides in D_2O to a concentration of about 8 mg mL^{-1}, and placing the solutions in a sealed cell composed of two CaF_2 windows separated by a 100 µm spacer. The spectra were obtained as averages of eight scans and corrected by subtraction of the solvent.

Calculations

Starting geometries of model smaller molecules were designed and optimized using the Gaussian16 program (Frisch et al. 2016). B3LYP (Becke 1993), B3PW91 (Perdew et al. 1996), CAM-B3LYP (Yanai et al. 2004), ωB97XD (Chai and Head-Gordon 2008), M062X (Zhao and Truhlar 2008), and BMK (Boese and Martin 2004) functionals were used, with the 6–31 + G** basis set and CPCM (Tomasi et al. 2005; Klamt and Schürmann 1993) or SMD (Marenich et al. 2009) solvent models with parameters of water. For the optimized geometries vibrational spectra were calculated at the same level using standard procedures for IR/VCD (Cheeseman et al. 1996) and Raman/ROA (Ruud and Thorvaldsen 2009; with 532 nm excitation). Calculations with different methods were used in order to test for the influence of functional on Raman intensity enhancement due to the pre-resonance phenomenon of the absorbing nitrotyrosine group.

For the peptides, starting geometries were obtained by molecular dynamics (MD) simulations performed using the Amber12 program (Case et al. 2012). Free dynamics of wild-type αSyn118-140 was run for 1 µs, with the Amber12SB force field. The peptide moved rather freely, with exception of the Pro128 residue. As an alternative to the free MD, we combined a 1 ns simulated annealing with subsequent 50 ns molecular dynamics simulations using the same force field (Niederhafner et al. 2019b). The trajectories were analyzed using the dictionary of secondary structures of proteins algorithm implemented in AmberTools.

From the MD trajectory, 33 snapshots were selected using a density-based clustering algorithm implemented in cpptraj

(AmberTools) with these parameters: minimum points for a cluster was set to 10, distance cutoff for forming a cluster (ε) was set to 1.9 Å (Figure S3), sieve to frame options was on, and coordinate root-mean-squared deviation distance metric was used with sieve 5 for all peptidic atoms except for hydrogens. Peptide geometries obtained from the clustering were used as starting structures in the DFT/HF calculations. The structures were partially optimized at the HF/STO-3G level with implicit CPCM water in vibrational normal mode coordinates, so that modes with frequency smaller than 200 cm^{-1} were fixed (Bouř and Keiderling 2002). Obtained peptide structures were further split to smaller fragments (Figure S4), which were also optimized in the normal mode coordinates using the same frequency limit, but at a higher level, B3LYP/6–31 + G**, with implicit CPCM water. For the optimized fragments, vibrational tensors at the B3LYP/6–31 + G** level were calculated and transferred back onto the full peptide, using the Cartesian coordinate tensor transfer (CCT) method (Bouř et al. 1997; Yamamoto and Bouř 2013). Then within the harmonic approximation IR and VCD intensities were calculated and the spectra plotted using Lorentzian bands and 10 cm^{-1} FWHH.

Results and discussion

Peptide synthesis

Preparation of nitrated peptides with total chemical synthesis provided uniform samples with specific tyrosine residues nitrated in only the 3-position (Niederhafner et al. 2016). In biological samples under oxidative stress, the nitration yield is far from 100% (Zhao et al. 2017; Radi 2013; Feeney and Schöneich 2013). However, our procedure can be viewed as that leading to 100% conversion.

The SERS Protocol

First small and cheap peptide models such as glutathione (GSH) and Met-enkephalin were investigated with SERS. Citrate stabilized silver nanoparticles were activated with 1 M HCl. The baseline after acidification (Figure S5) mostly reflected water scattering, i.e. the citrate vibrations were suppressed. The presence of strong acids probably disturbed the anionic Langmuir layer around the colloid and exposed the surface towards analyte. This led to amplification of analyte SERS without interference of signals from colloid stabilizing anions (Figure S5f). After spectra of pure colloids were subtracted, SERS spectra of the peptides (at ~ 10^{-5} M) were obtained and are shown in Fig. 2b, d. As usual, the relative intensities in SERS differed from non-enhanced Raman for these analytes (measured at much higher concentrations, ~ 10^{-1} M). The 10^4 difference in concentration

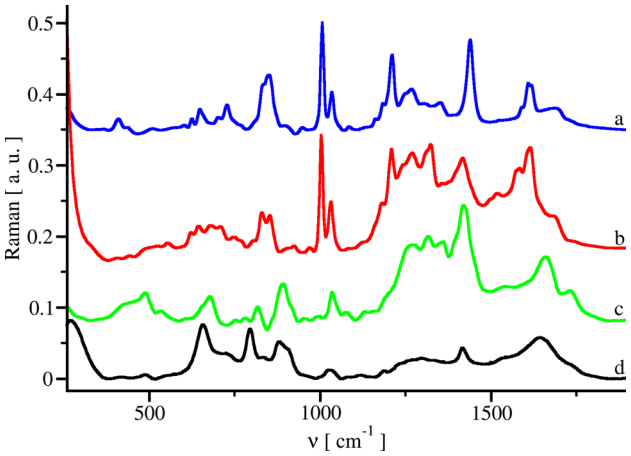

Fig. 2 Raman (**a, c**) and SERS (**b, d**) spectra of GSH (**c, d**) and Met-enkephalin (**a, b**). Experimental conditions: **a** laser power (lp) 570 mW, illumination time (it) 1616 min, 1.2×10^{-1} mol/L; **b** lp 200 mW, it 5.23 min, 1.2×10^{-5} mol/L; **c** lp 970 mW, it 906 min, 4×10^{-1} mol/L; **d** lp 200 mW, it 3.73 min, 1.2×10^{-5} mol/L. To reasonably compare the spectra, the intensities were scaled dividing by 1.2×10^{11} (**a**), 2.7×10^{8} (**b**), 6.7×10^{10} (**c**), and 6.2×10^{7} (**d**)

between SERS and Raman measurements is needed due to the low sensitivity of the ordinary Raman method and the enhanced sensitivity of SERS resulting from plasmon coupling to the Ag colloidal particles. The variation in enhancement for different vibrational bands has been attributed to different chromophore distance or orientation to the surface (Novák et al. 2012), or even to a chemical reaction at the surface (Huang et al. 2010; Sun and Xu 2012; Novák et al. 2016; Cho et al. 2017).

We also compared various silver colloids stabilized with citrate and borate. The borate ones exhibited extra SERS signals in the region of the asymmetric NO_2 stretching ($\nu_{NO2,as}$, 1550–1475 cm^{-1}), and were therefore not studied further (Fig. 3f). The spectra of citrate based colloids were sensitive to the presence of Nit in the peptide chain, that is they contained the δ_{NO2} and $\nu_{NO2,as}$ bands at 828–880 cm^{-1} and 1550–1475 cm^{-1}, respectively. Because the $\nu_{NO2,s}$ band (1360–1290 cm^{-1}) is almost always overlapped with other peptidic bands, it is not so useful for detection of protein tyrosine nitration (Figs. 3, 4, S6, and S7). By contrast, while the $\nu_{NO2,as}$ band is usually weak, it can be used as an important marker indicating peptides nitrated at tyrosine. Another indicator can be observed in the δ_{NO2} region (828–880 cm^{-1}) overlapping with a tyrosine double band [around 825–870 cm^{-1} (Tuma 2005; Rygula et al. 2013), out-of-plane H-C bend (η_{HC}, 825 cm^{-1}) and ring breathing (β_{CCC}, 850 cm^{-1})]. After nitration, the relative magnitudes of the two bands become opposite (i.e. "big-small" as seen in Fig. 3b, g; Fig. 4a, b–h; Figure S6, a and b–d) due to overlap with δ_{NO2} signal and further perturbation of the benzene ring symmetry.

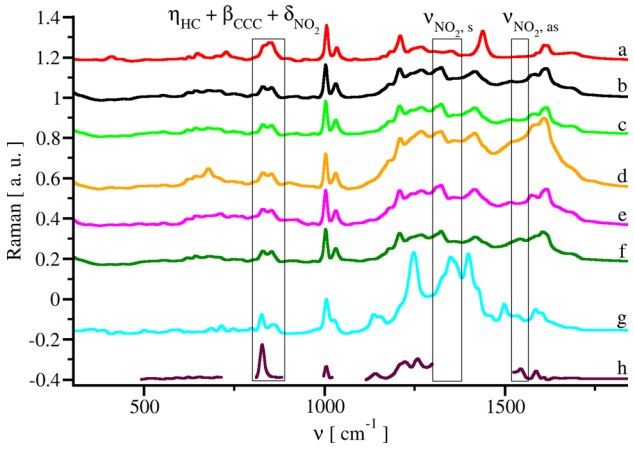

Fig. 3 SERS and Raman spectra of Met-enkephalin with various colloids (**b–f**): **b** sol **19c**, **c** sol **19b**, **d** sol **19a**, **e** sol **19d**, **f** sol **18**, **g** sol **19c**. Raman of Met-enkephalin (**a**). SERS of [Nit^1]Met-enkephalin (**g**). Raman of [Nit^1]Met-enkephalin in 50% CH_3CN/H_2O (**h**). Experimental conditions: **a** laser power (lp) 570 mW, illumination time (it) 1616 min, 1.2×10^{-1} mol/L; **b–f** lp 200 mW, it 5.23 min, 1.2×10^{-5} mol/L; **g** lp 200 mW, it 10.4 min, 1.2×10^{-5} mol/L; **h** lp 200 mW, it 47 min, 2.58×10^{-2} mol/L in 50% CH_3CN/H_2O. Measured intensities were divided by 9×10^{10} (**a**), 2×10^{8} (**b–f**), 3.5×10^{8} (**g**) and 1.0×10^{9} (**h**) for the presentation

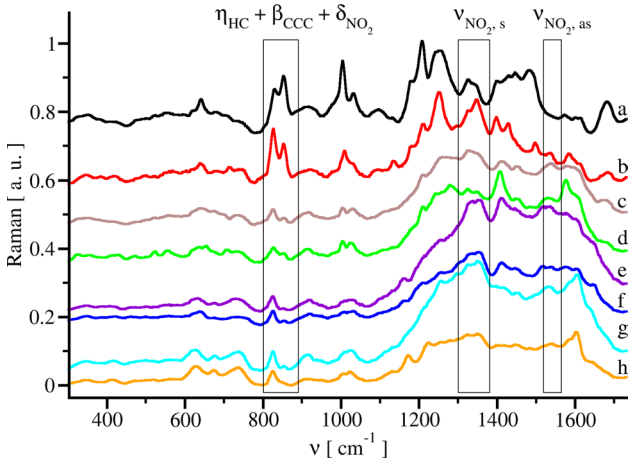

Fig. 4 SERS spectra of αSyn118-140 and its selected nitro derivatives: **a** αSyn118-140, **b** [Nit^{125}]αSyn118-140, **c** [Nit^{133}]αSyn118-140, **d** [Nit^{136}]αSyn118-140, **e** [Nit^{125,133}]αSyn118-140, **f** [Nit^{125,136}]αSyn118-140, **g** [Nit^{133,136}]αSyn118-140, and **h** [Nit^{125,133,136}]αSyn118-140. Experimental conditions: **a** lp 200 mW, it 9.0 min, 1.2×10^{-5} mol/L; **b** lp 200 mW, it 6.7 min, 1.2×10^{-5} mol/L; **c** lp 200 mW, it 14.9 min, 1.2×10^{-5} mol/L; **d** lp 200 mW, it 6.7 min, 1.2×10^{-5} mol/L; **e** lp 200 mW, it 6.7 min, 1.2×10^{-5} mol/L; **f** lp 200 mW, it 9.7 min, 1.2×10^{-5} mol/L; **g** lp 200 mW, it 32.9 min, 1.2×10^{-5} mol/L; **h** lp 200 mW, it 9.0 min, 1.2×10^{-5} mol/L. Intensities were divided by 5.9×10^{7} (**a**), 7.1×10^{7} (**b**), 5.0×10^{7} (**c**), 7.8×10^{7} (**d**), 2.5×10^{8} (**e**), 2.0×10^{8} (**f**), 1.7×10^{8} (**g**) and 2.5×10^{8} (**h**)

In the Raman spectrum of [Nit^1]Met-enkephalin, the δ_{NO2} signal dominates within the Met-enkephalin bands between 825–870 cm^{-1} (Fig. 3h compared to Fig. 3a). In SERS, this intensity change is less dramatic (compare Fig. 3b, g), but the δ_{NO2} vibration becomes dominant when most of the Tyr residues are nitrated (compare single NO_2 labels in Fig. 4c–d with double and triple NO_2 labels in Fig. 4e–h).

Vibrational band assignment

The intensities of β_{CCC}, η_{HC}, and δ_{NO2} bands somewhat contradict the analysis of nitrated tyrosine models based on 2-nitrophenol (Quaroni and Smith 1999b). To verify band assignments, we used a model of Nit – 4-methyl-2-nitrophenol, where the aliphatic part of tyrosine is represented by a methyl group instead of hydrogen (Fig. 5). The methyl group is a closer model than is H to the positive inductive effect of the aliphatic part of tyrosine.

First, by comparison of phenol and *p*-cresol spectra, with that of their nitrated derivatives, we investigated the vibrations of aromatic systems in the region 825–870 cm^{-1}, which are characteristic for peptides containing Tyr. According to DFT calculations for the model, characteristic vibrations in phenol at 814 cm^{-1} (β_{CCC}) and 829 cm^{-1} (η_{HC}) are moved to 825 cm^{-1} (η_{HC}) and 843 cm^{-1} (β_{CCC}) in *p*-cresol (cf. spectra a and e). Relative intensities in the 825 and- 870 cm^{-1} range strongly vary after nitration. For example, phenol nitration affects combinations of the in-phase and out-of-phase modes of ring vibrations with δ_{NO2} and the splitting of the peaks at 820 cm^{-1} ($\beta_{CCC}+\delta_{NO2}$) and 872 cm^{-1} (out-of-phase $rv+\delta_{NO2}$) (cf. spectra in Fig. 5a compared to Fig. 5b, c). The intensity of η_{HC} becomes negligible. Experimentally, the intensities differ between solid and molten states (b and c). The situation is different in 4-cresol and 4-methyl-2-nitrophenol (e and d). The signal in this region is transformed to double peaks with wavenumbers 776 cm^{-1} and 825 cm^{-1}. The 825 cm^{-1} combination mode of β_{CCC} and δ_{NO2} vibrations is very intense and overlaps with a band of the cresol. The 776 cm^{-1} band is a mix of ring vibrations with δ_{NO2} and is weaker than the vibration around 825 cm^{-1}. In the presence of both nitrotyrosines and tyrosines, we can usually see increase of the intensity around 825 cm^{-1} caused by the tyrosine η_{HC} and nitrotyrosine β_{CCC} and δ_{NO2} vibrations.

The spectra of *p*-cresol and 4-methyl-2-nitrophenol are reasonably well reproduced by DFT (Figs. 6 and S8). The calculation suggests that the liquid 4-methyl-2-nitrophenol predominantly adopts a conformer with an in-plane intramolecular hydrogen bond (Fig. 6). Detailed assignment of *p*-cresol and 4-methyl-2-nitrophenol bands is in Table S1.

Formation of azobenzenes

During the SERS measurements we observed spectral changes which were interpreted as a conversion of *o*-nitrophenolates to corresponding azobenzenes on the silver surface (Figs. 7 and 8). Such a transformation has already been

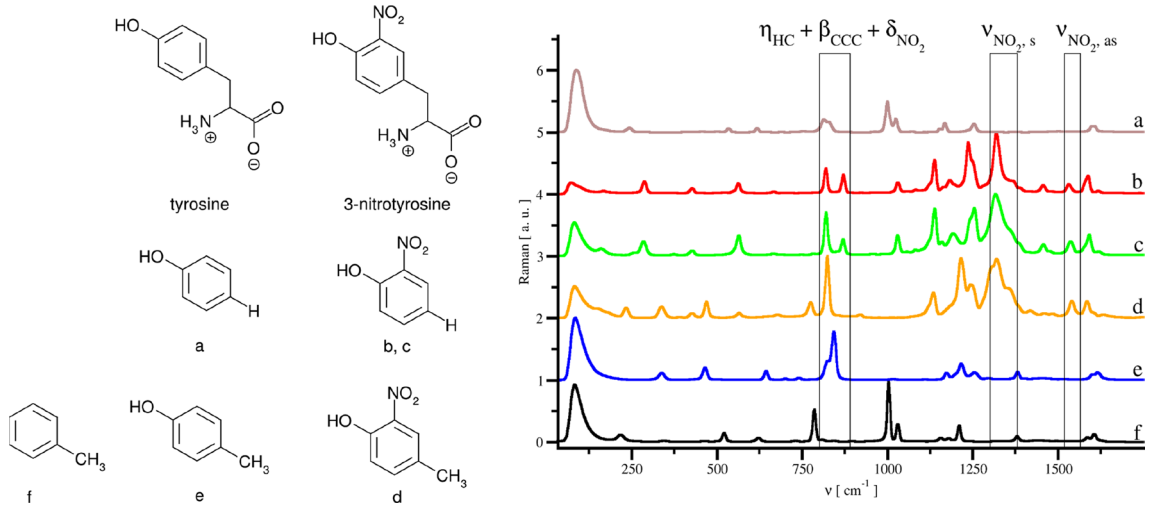

Fig. 5 Structures and experimental neat sample Raman spectra of model systems demonstrating the changes after nitration of phenol and *p*-cresol. **a** phenol (solid, 25 °C); **b** 2-nitrophenol (solid, 25 °C); **c** 2-nitrophenol (liquid, 45 °C); **d** 4-methyl-2-nitrophenol (liquid, 40 °C); **e** *p*-cresol (liquid, 40 °C); and **f** toluene (liquid, 25 °C). Laser powers/illumination times/intensities divided by: 50 mW/38.5 min/5.1×10^9 (**a**), 20 mW/1.6 min/1.9×10^8 (**b**), 20 mW/1.6 min/3.2×10^8 (**c**), 16 mW/1.6 min/2.0×10^8 (**d**), 70 mW/1.6 min/4.1×10^8 (**e**), 50 mW/11.1 min/2.1×10^9, all neat samples

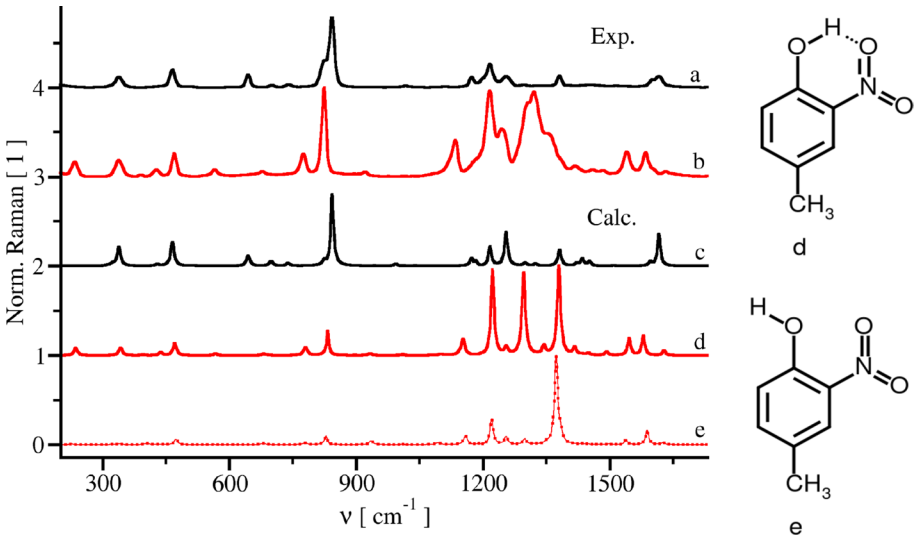

Fig. 6 Experimental and calculated Raman spectra of *p*-cresol (liquid, black, **a, c**) and 4-methyl-2-nitrophenol (liquid, red, **b, d, e**). Parameters of calculations: CAM-B3LYP functional, 6–31 + G** basis set, water CPCM model, Akima scaling function. The two conformers of 4-methyl-2-nitrophenol differ in presence (**d**) and absence (**e**) of the intramolecular hydrogen bond (**d**)

observed by others (Huang et al. 2010; Sun and Xu 2012; Novák et al. 2016; Cho et al. 2017) on similar substrates including *p*-nitrothiophenolates. During the reaction, the nitro group is decomposed and the δ_{NO2} and $\nu_{NO2,as}$ bands partially vanish (Fig. 7, a and b). The ν_{C-C} and ν_{C-N} intensities at 1028 cm^{-1} of nitrotyrosine also decrease (1030 cm^{-1}, Quaroni and Smith 1999b). A new strong band grows at 1398 cm^{-1} (Fig. 7d), in a parallel to previous observations of the $\nu_{N=N}$ vibration at 1381, 1388 or 1389 cm^{-1} when azobenzene is formed from *p*-aminothiophenole derivatives (Huang et al. 2010; Sun and Xu 2012; Novák et al. 2016; Cho et al. 2017). Similarly, in our spectrum an increased intensity occurs at 1156 cm^{-1}, which could correlate to the CN stretch of azobenzene observed at 1143 cm^{-1} (Stuart et al. 2007). The azobenzene can exist in cis and trans forms, and for cis-azobenzene an intense peak at 275 cm^{-1} corresponding to CCNN torsion was observed (Stuart et al. 2007). In our experiments an intense peak at 238 cm^{-1} grew in for about 7 min and then diminished. We attribute this to a two-step process, interconversion of the nitrotyrosine to *cis*-hydroxyazobenzene, followed by the cis–trans isomerization. This can be corroborated by observation of the growing in of a band at 1499 cm^{-1} corresponding to the *trans*-azobenzene CC stretch (1492 cm^{-1}, Stuart et al. 2007). A small band at 1601 cm^{-1} corresponds to CC stretches of both azobenzene isomers (1592 cm^{-1}, Stuart et al. 2007).

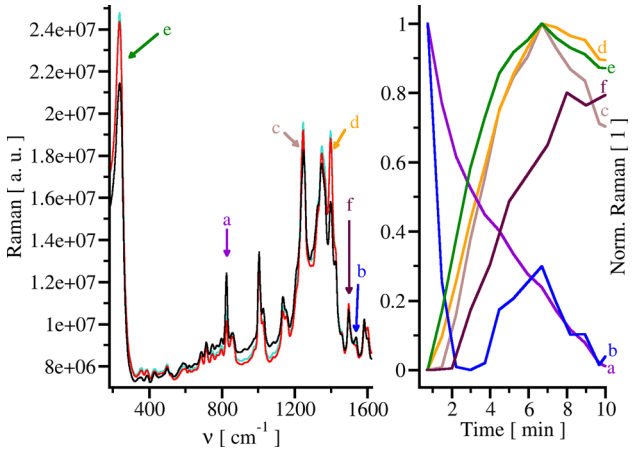

Fig. 7 SERS spectral changes attributed to the formation of azobenzene after binding of [Nit^1]Met-enkephalin to the silver surface. The left panel contains spectra after the first set of 32 scans (black) and the last 416 scans (red, the intensity is normalized to one cycle of 32 scans), on the right intensities of selected bands (**a–f**) are plotted. The cyan spectrum represents the state at 7 min from the right panel, i.e. with higher signal of azobenzene after 256 scans. The δ_{NO2} bands at 825 cm^{-1} (**a**) and $\nu_{NO2,as}$ at 1538 cm^{-1} (**b**) are decreasing with time, while the bands at 1249 cm^{-1} (**c**), ν(N=N) 1398 cm^{-1} (**d**), 238 cm^{-1} (**e**, CCNN torsion of *cis*-azobenzene), and 1499 cm^{-1} (**f**, CC stretch of *trans*-azobenzene) characteristic for azobenzenes are growing

Limitations of SERS technique

SERS is more useful for qualitative measurement, since quantification depends on binding of the peptides to the surface (transport limitations). The changes of absorbance during the SERS measurement and parasitic fluorescence require added signal processing and normalization in order to quantitatively compare experiments. We have determined the limit of detection (LOD) of [Nit^1]Met-enkephalin by SERS to be above 0.5 µmol L^{-1} (Fig. 9). While MS techniques, in particular, can reach much lower detection limits for monitoring PTM (Tsikas and Duncan 2014), our methods were not optimized for LOD, and with designed plasmonic substrates one can improve LOD for SERS (Stiles et al. 2008; Zhang et al. 2014a, b; Betz et al. 2014; Kleinman et al. 2013) and apply it for detection of Nit formation. The reproducibility in the region of tyrosine specific vibration (825–875 cm^{-1}) is very high, and even changes of nanoparticles batch do not interfere with observed pattern (see also Fig. 3). The only tricky part is the synthesis of silver seed **18**, where the reproducibility of getting stable seeds is ca 20–25%. It is very sensitive to mixing of the two reagents and one of them, $NaBH_4$, is strongly hygroscopic. From a preparation of five batches, typically one precipitated out by the second day, and three more within a week. The last is often then stable for several months at 4 °C, while avoiding strong light and shaking. On the other hand, the conversion of these seeds to SERS active particles **19** is very reproducible.

Effect of the nitration on peptide properties

The nitration significantly lowered the peptide solubility in water. For instance, non-enhanced Raman spectra of Met-enkephalin could be measured in water, whereas [Nit^1]Met-enkephalin needed to be dissolved in an acetonitrile/water 1:1 mixture. On the other hand, SERS spectra of both samples could be obtained in water, due to significantly lower limit of detection of SERS in comparison to that of Raman spectroscopy. Similar solubility limitations were observed for peptides from the αSyn118-140 series, where the non-nitrated peptide was soluble enough for measurement of VCD spectra in D_2O. Mono-nitration at position 125 and

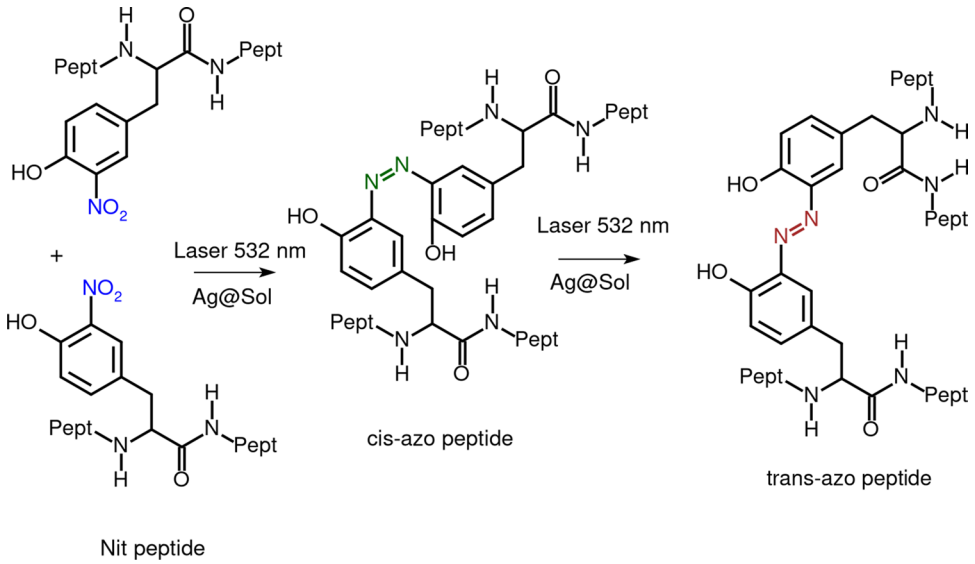

Fig. 8 Suggested cross-linking of the peptides under formation of the azobenzenes during the SERS measurement

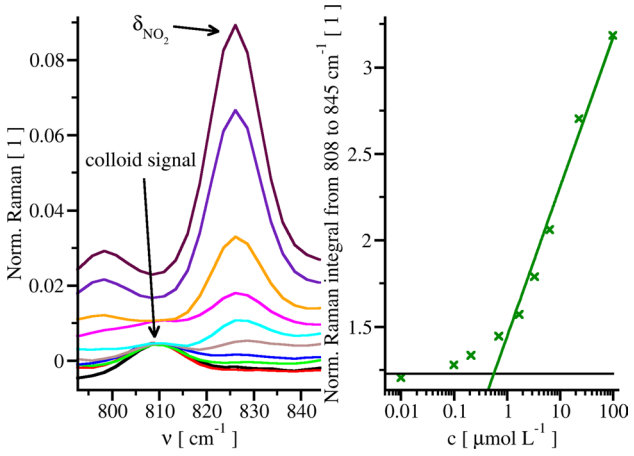

Fig. 9 Dependence of normalized SERS signal shape (left) and intensity (right) of [Nit[1]]Met-enkephalin on concentration. Intersection of correlation function with integral value at zero concentration is at ca 0.5 µmol L^{-1}. Spectra were normalized to the same intensity of vibration of water at 84 cm^{-1} after the fluorescence suppression using Akima spline fitted to these anchoring points: 42, 323, 337, 373, 535, 599, 787, 872, 942, 982, 1059, 1485, 1835, 1929, 2073, 2300, and 2318 cm^{-1}. Concentration of analyte in the left spectra: 0 (black), 0.01 (red), 0.1 (green), 0.21 (blue), 0.7 (brown), 1.7 (cyan), 3.3 (magenta), 6.4 (orange), 23 (indigo), 100 (maroon) µmol L^{-1}

136 as well as dinitration at positions 125 and 136 did not affect the solubility of αSyn118-140 and VCD spectra could also be acquired in water. However, any other nitrations led to very limited solubility in water and prevented accumulation of VCD, Raman, and ROA spectra.

ECD spectra for all αSyn118-140 models acquired at lower concentrations (Figure S9) exhibit a negative minimum at 198 nm, consistent with a disordered structure. At the higher concentrations, the IR and VCD spectra of the unlabeled and singly nitrated αSyn118-140 models also indicate a disordered conformation. However, dinitration of αSyn118-140 at Tyr125 and Tyr136 led to dramatic changes in the VCD spectrum (cf blue line with others, Fig. 10C), that correspond to a transition from a disordered to aggregated state (accompanied by an increase of β-sheet conformation). Indeed, partial precipitation of the sample was also observed. The formation of a β-sheet aggregate is confirmed by the IR spectra exhibiting a splitting in the amide I band (Fig. 10A, peaks f and g). In IR, the $\nu_{NO2,as}$ signal at 1531 cm^{-1} is close to a tyrosine ring band at 1516 cm^{-1} (Venyaminov and Kalnin 1990; Rahmelow et al. 1998; Quaroni and Smith 1999b). The ratio of IR peaks at 1516 cm^{-1} and 1531 cm^{-1} can indicate the amount of nitro groups (cf. spectra b, c with d, e, Fig. 10A).

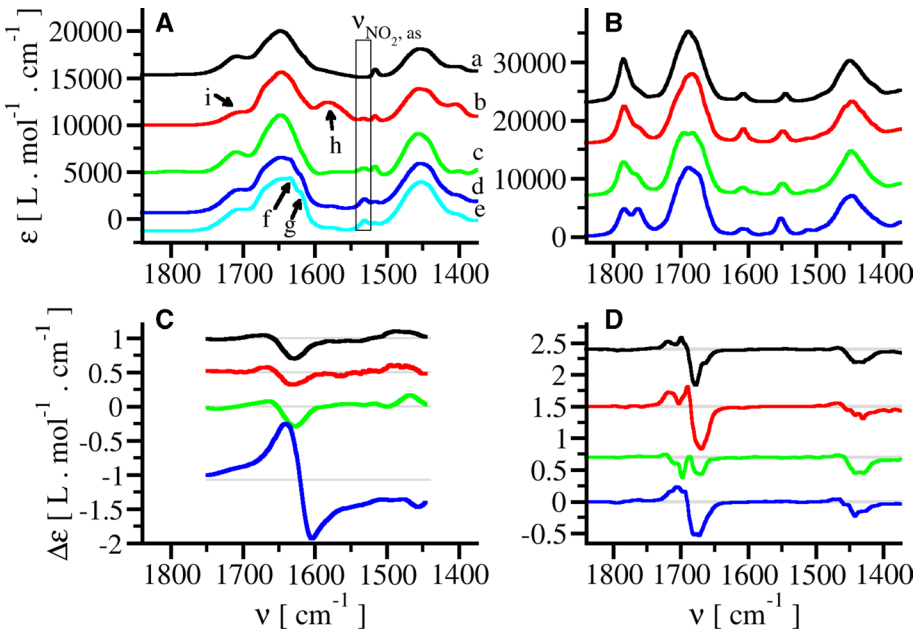

Fig. 10 Experimental (**A**, **C**) and calculated (**B**, **D**) IR (**A**, **B**) and VCD (**C**, **D**) spectra of αSyn118-140 peptide derivatives: **a** αSyn118-140 (black), **b** [Nit^{125}]αSyn118-140 (red), **c** [Nit^{136}]αSyn118-140 (green), **d** [$Nit^{125,136}$]αSyn118-140 (blue), and **e** [$Nit^{125,136}$]αSyn118-140. Spectra **A–d** were measured before VCD experiments, whereas the IR spectrum **A–e** corresponds to the state after VCD experiment. The increase of the intensities at 1634 cm^{-1} (**f**) and 1620 cm^{-1} (**g**) can indicate some aggregation of the peptide during measurement, which is not accounted for in the calculated spectra. Due to higher *pD* ~ 4.6, two forms of carboxylic group are observed COO^- (**h**) and COOH (**i**). Experimental VCD were smoothed

Peptide secondary structure

To understand possible changes in conformational behavior caused by the dinitration, we have carried out MD of these peptides. Example snapshot geometries are plotted in Fig. 11. Although the molecules are quite flexible, secondary structure analysis suggests that the nitration causes changes even in the conformation of the main peptide chain (Figure S10 and S11). For example, β-turn motif between residues 129–135 (12–18 in Figures S10 and S11) becomes less frequent in the 125 and 133 mutants of αSyn118-140. The least polar 125 mutant does not form the α-helix at all. Mostly, the spectra are rather similar, except for [Nit^{125,136}]αSyn118-140 which differs in IR and VCD due to aggregation (Fig. 10A, C).

Experimental and calculated IR and VCD spectra are compared in Fig. 10, minor changes of computational parameters are explored in Figures S12 and S13. As usual, calculated frequencies differed from the experimental ones, but the shapes mostly resemble the experiment. In the calculated IR spectra, COOH side-chain vibration corresponding to the 1709 cm^{-1} experimental band is missing as it was omitted in spectral simulations (Figure S13, panels C and D). Comparison of spectra in panels C and D combined with vibrational analysis revealed that predicted aromatic vibrations are overlapped with predicted amide I' and II' vibrations. When dimeric full fragments that include the side-chain carboxylic groups were used to model the larger peptide by use of CCT (Figure S13, panels E and F), the COOH band was reproduced. Because the number of MD snapshots had to be limited (to 33 conformers of αSyn118-140 models), the bands at 1783 and 1763 cm^{-1} are unrealistically split (cf. Figure 10A, B). Experimentally, only one band is present. The tyrosine vibration (exp. at 1516 cm^{-1}) is also reproduced, at 1545 cm^{-1}. The calculated $\nu_{NO2,as}$ at ca 1556 cm^{-1} is overlapping with calculated tyrosine ring vibration at 1545 cm^{-1}. This led to shift of the calculated tyrosine band to higher wavenumbers with increasing nitration: 1545 cm^{-1} wild-type (Fig. 10B, black), 1549 cm^{-1} mono-nitro (Fig. 10B, red and green), to 1552 cm^{-1} dinitro (Fig. 10B, blue). For dinitration, the intensity of this band was also slightly increased. The calculated nitrophenolic ring vibrations at ca 1440 and 1670 cm^{-1} are overlapping with calculated amide II' (1448 cm^{-1}) and amide I' (1687 cm^{-1}), respectively.

Possible conformers of the αSyn25-53 peptide are documented on the MD snapshots in Figs. 12 and S14. The snapshots are only illustrative, since the helical fraction in the MD trajectory is below 4% and the position of α-helical fragments shift during the simulation i.e. none of the residues is permanently α-helical. The negative ECD minimum at 198 nm for αSyn25-53 is more intense than for the αSyn118-140 series (Figures S9 and S15); however the shape is similar and in both cases the disordered structure is dominant. This is in a good agreement with experimental IR

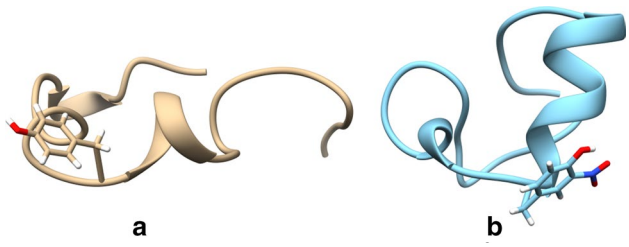

Fig. 12 **a** αSyn25-53 and **b** [Nit^{39}]αSyn25-53, snapshots from MD

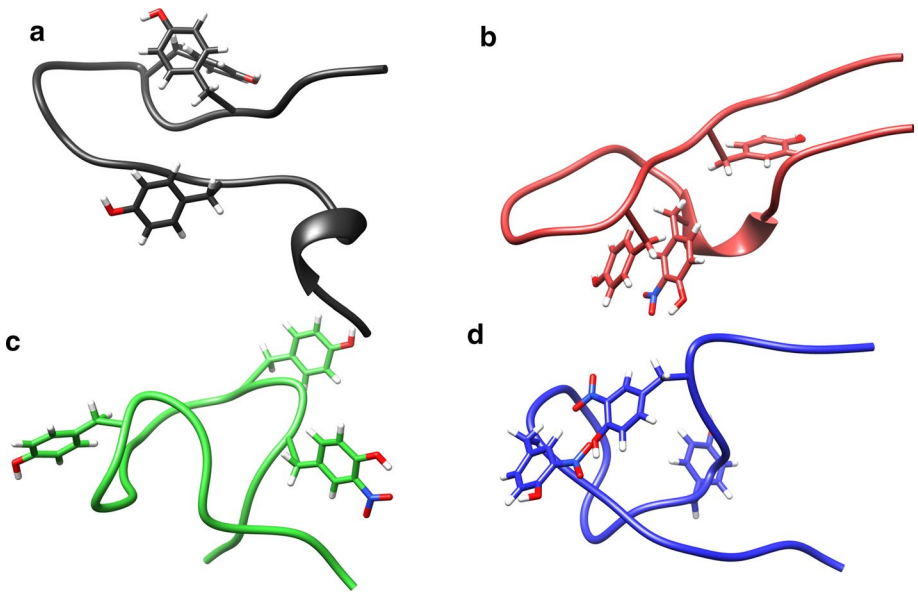

Fig. 11 **a** αSyn118-140, **b** [Nit^{125}]αSyn118-140, **c** [Nit^{136}]αSyn118-140, and **d** [Nit^{125,136}]αSyn118-140, snapshots from MD

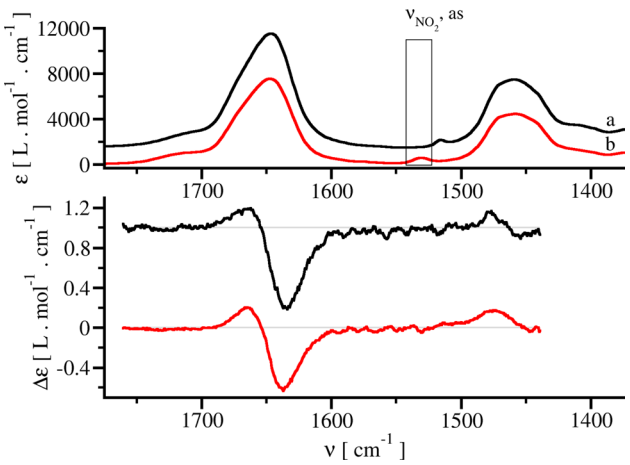

Fig. 13 Experimental IR and VCD spectra of peptides from αSyn25-53 series. **a** αSyn25-53 and **b** [Nit^{39}]αSyn25-53

and VCD spectra (Fig. 13), where a (+, −) couplet, typical for disordered peptides, is observed at 1664 and 1635 cm^{-1}. Thus for αSyn25-53 peptides, the nitration did not significantly influence the predominantly disordered secondary structure.

Conclusion

We have developed a SERS measurement protocol suitable for qualitative detection of protein tyrosine nitration, and tested it on model in Met-Enkephalin, rev-Prion protein, and α-Synuclein systems. Useful marker bands were identified, such as a characteristic double peak of tyrosine residue around 825–870 cm^{-1} altered by the bending vibration of the nitro group serves as an important marker of the nitration. The relative intensities change from "small-big" in natural peptide to "big-small" after the nitration. By a detailed analysis of the time-dependence of the spectra, we also found that the laser light during the SERS measurement can induce conversion of the nitrotyrosine to azobenzene containing peptides. This could be related to previous experiments and should be accounted for in interpreting SERS data. The DFT and MD computations and further spectroscopies (VCD, IR, ECD) provided useful background data for the interpretation of the SERS intensities and peptide behavior. For the DFT modeling the best performing functionals were CAM-B3LYP and ωB97XD. All conformational analyses and spectroscopic methods suggest that the nitration of α-synuclein models does not significantly influence the conformation but changes the solubility and aggregation properties. The double nitration at 125 and 136 position of αSyn118-140 causes the largest changes in the behavior of the peptide. These optical spectroscopies thus significantly contribute to our understanding of peptide behavior related to the oxidative stress and consequent tyrosine nitration.

Acknowledgements This work was supported by the Czech Science Foundation (14-00431S, 17-00121S, 20-10144S), Research Project RVO 61388963, by European Regional Development Fund; OP RDE; Project: "Chemical biology for drugging undruggable targets (ChemBioDrug)" (No. CZ.02.1.01/0.0/0.0/16_019/0000729), and computational grants of CESNET (LM2015042) and the CERIT-SC (LM2015085).

Compliance with ethical standards

Conflict of interest Authors declare that they have no conflict of interest.

Human participants or animals This paper does not contain any studies with human participants or animals performed by any of the authors. For this type of study formal consent is not required.

References

Abello N, Kerstjens HA, Postma DS, Bischoff R (2009) Protein tyrosine nitration: Selectivity, physicochemical and biological consequences, dinitration and proteomic methods for the identification of tyrosine-nitrated proteins. J Proteome Res 8(7):3222–3238

Alvarez-Puebla RA, Contreras-Caceres R, Pastoriza-Santos I, Perez-Juste J, Liz-Marzan LM (2009) Au@pNIPAM colloids as a molecular traps for surface-enhanced, spectroscopic, ultra-sensitive analysis. Angew Chem Int Ed 48(1):138–143

Anderson JP, Walker DE, Goldstein JM, de Laat R, Banducci K, Caccavello RJ, Barbour R, Huang J, Kling K, Lee M, Diep L, Keim PS, Shen X, Chataway T, Schlossmacher MG, Seubert P, Schenk D, Sinha S, Gai WP, Chilcote TJ (2006) Phosphorylation of Ser-129 is the dominant pathological modification of alpha-synuclein in familial and sporadic Lewy body disease. J Biol Chem 281:29739–29752

Aslan M, Dogan S (2011) Proteomic detection of nitroproteins as potential biomarkers for cardiovascular disease. J Proteomics 74(11):2274–2288

Barron LD (2012) From cosmic chirality to protein structure: Lord Kelvin's legacy. Chirality 24(11):879–893

Barron LD, Buckingham AD (2010) Vibrational optical activity. Chem Phys Lett 492(4–6):199–213

Barron LD, Hecht L, Blanch EW, Bell AF (2000) Solution structure and dynamics of biomolecules from Raman optical activity. Prog Biophys Mol Biol 73(1):1–49

Barron LD, Hecht L, McColl IH, Blanch EW (2004) Raman optical activity comes of age. Mol Phys 102(8):731–744

Barron LD, Zhu F, Hecht L (2006) Raman optical activity: An incisive probe of chirality, and of biomolecular structure and behaviour. Vib Spectrosc 42(1):15–24

Becke AD (1993) Density-functional thermochemistry. III. The role of exact exchange. J Chem Phys 98(7):5648–5652

Beckman JS, Crow JP (1993) Pathological implications of nitric oxide, superoxide and peroxynitrite formation. Biochem Soc Trans 21(2):330–334

Beckman JS, Beckman TW, Chen J, Marshall PA, Freeman BA (1990) Apparent hydroxyl radical production by peroxynitrite: Implications for endothelial injury from nitric oxide and superoxide. Proc Natl Acad Sci USA 87(4):1620–1624

Betz JF, Yu WW, Cheng Y, White IM, Rubloff GW (2014) Simple SERS substrates: powerful, portable, and full of potential. Phys Chem Chem Phys 16(6):2224–2239

Bodanszky M, Bodanszky A (1994) The practice of peptide synthesis. Springer, Berlin, p 48

Boese AD, Martin JML (2004) Development of density functionals for thermochemical kinetics. J Chem Phys 121(8):3405–3416

Bouř P, Keiderling TA (2002) Partial optimization of molecular geometry in normal coordinates and use as a tool for simulation of vibrational spectra. J Chem Phys 117(9):4126–4132

Bouř P, Sopková J, Bednarová L, Maloň P, Keiderling TA (1997) Transfer of molecular property tensors in cartesian coordinates: a new algorithm for simulation of vibrational spectra. J Comput Chem 18(5):646–659

Burai R, Ait-Bouziad N, Chiki A, Lashuel HA (2015) Elucidating the role of site-specific nitration of α-synuclein in the pathogenesis of Parkinson's disease via protein semisynthesis and mutagenesis. J Am Chem Soc 137(15):5041–5052

Campolo N, Issoglio FM, Estrin DA, Bartesaghi S, Radi R (2020) 3-Nitrotyrosine and related derivatives in proteins: precursors, radical intermediates and impact in function. Essays Biochem 64(1):111–133

Case DA et al (2012) AMBER 12. University of California, San Francisco

Castro L, Demicheli V, Tortora V, Radi R (2011) Mitochondrial protein tyrosine nitration. Free Radic Res 45(1):37–52

Chai J-D, Head-Gordon M (2008) Long-range corrected hybrid density functionals with damped atom-atom dispersion corrections. Phys Chem Chem Phys 10(44):6615–6620

Cheeseman JR, Frisch MJ, Devlin FJ, Stephens PJ (1996) Ab Initio calculation of atomic axial tensors and vibrational rotational strengths using density functional theory. Chem Phys Lett 252(3–4):211–220

Cho FH, Kuo SC, Lai YH (2017) Surface-plasmon-induced azo coupling reaction between nitro compounds on dendritic silver monitored by surface-enhanced Raman spectroscopy. RSC Adv 7(17):10259–10265

Di Bello C, Griffin JH (1975) Circular dichroism and absorbance properties of nitrotyrosyl chromophores in staphylococcal nuclease and in a model diketopiperazine. J Biol Chem 250:1445–1450

Duda JE, Giasson BI, Chen Q, Gur TL, Hurtig HI, Stern MB, Gollomp SM, Ischiropoulos H, Lee VM, Trojanowski JQ (2000) Widespread nitration of pathological inclusions in neurodegenerative synucleinopathies. Am J Pathol 157(5):1439–1445

Erickson BW, Merrifield RB (1973) Acid stability of several benzylic protecting groups used in solid-phase peptide synthesis. Rearrangement of O-benzyltyrosine to 3-benzyltyrosine. J Am Chem Soc 95(11):3750–3756

Feeney MB, Schöneich Ch (2013) Proteomic approaches to analyze protein tyrosine nitration. Antioxid Redox Signal 19(11):1247–1256

Fields GB, Noble RL (1990) Solid phase peptide synthesis utilizing 9-fluorenylmethoxycarbonyl amino acids. Int J Pept Prot Res 35(3):161–214

Frisch MJ et al (2016) Gaussian 16 revision A.03. Gaussian, Inc., Wallingford CT

Fujiwara H, Hasegawa M, Dohmae N, Kawashima A, Masliah E, Goldberg MS, Shen J, Takio K, Iwatsubo T (2002) Alpha-Synuclein is phosphorylated in synucleinopathy lesions. Nat Cell Biol 4:160–164

Giasson BI, Duda JE, Murray IVJ, Chen Q, Souza JM, Hurtig HI, Ischiropoulos H, Trojanowski JQ, Lee VM-Y (2000) Oxidative damage linked to neurodegeneration by selective α-synuclein nitration in synucleinopathy lesions. Science 290(5493):985–989

Graham D, Thompson DG, Smith WE, Faulds K (2008) Control of enhanced Raman scattering using a DNA-based assembly process of dye-coded nanoparticles. Nat Nanotechnol 3(9):548–551

Guerrini L, Graham D (2012) Molecularly-mediated assemblies of plasmonic nanoparticles for Surface-Enhanced Raman spectroscopy applications. Chem Soc Rev 41:7085–7107

Gurry T, Ullman O, Fisher CK, Perovic I, Pochapsky T, Stultz CM (2013) The dynamic structure of α-synuclein multimers. J Am Chem Soc 135(10):3865–3872

Huang YF, Zhu HP, Liu GK, Wu DY, Ren B, Tian ZQ (2010) When the signal is not from the original molecule to be detected: chemical transformation of para-aminothiophenol on Ag during the SERS measurement. J Am Chem Soc 132(27):9244–9246

Hudecová J, Horníček J, Buděšínský M, Šebestík J, Šafařík M, Zhang G, Keiderling TA, Bouř P (2012) Three types of induced tryptophan optical activity compared in model dipeptides: theory and experiment. Chem Phys Chem 13(11):2748–2760

Ischiropoulos H, Zhu L, Chen J, Tsai M, Martin JC, Smith CD (1992) Peroxynitrite-mediated tyrosine nitration catalyzed by superoxide dismutase. Arch Biochem Biophys 298(2):431–437

Izzo GE, Jordan F, Mendelsohn R (1982) Resonance Raman and 500-MHz ^{1}H NMR Studies of tyrosine modification in hen egg white lysozyme. J Am Chem Soc 104(11):3178–3182

Ježek J, Hlaváček J, Šebestík J (2017) Applications for treatment of neurodegenerative diseases. Prog Drug Res 72:99–134

Jing H, Zhang Q, Large N, Yu C, Blom DA, Nordlander P, Wang H (2014) Tunable plasmonic nanoparticles with catalytically active high-index facets. Nano Lett 14(6):3674–3682

Keiderling TA (2020) Structure of condensed phase peptides: insights from vibrational circular dichroism and raman optical activity techniques. Chem Rev 120(7):3381–3419

Keiderling TA, Lakhani A (2018) Mini review: Instrumentation for vibrational circular dichroism spetroscopy, still a role for dispersive instruments. Chirality 30(3):238–253

Kessler J, Andrushchenko V, Kapitán J, Bouř P (2018) Insight into vibrational circular dichroism of proteins by density functional modeling. Phys Chem Chem Phys 20:4926–4935

Klamt A, Schürmann G (1993) COSMO: a new approach to dielectric screening in solvents with explicit expressions for the screening energy and its gradient. J Chem Soc Perkin Trans A 2(5):799–805

Kleinman SL, Frontiera RR, Henry AI, Dieringer JA, Van Duyne RP (2013) Creating, characterizing and controlling chemistry with SERS hot spots. Phys Chem Chem Phys 15(1):21–36

Krajnik M, Schäfer M, Sobanski P, Kowalewski J, Bloch-Boguslawska E, Zylicz Z, Mousa SA (2010) Enkephalin, its precursor, processing enzymes, and receptor as part of a local opioid network throughout the respiratory system of lung cancer patients. Human Pathol 41(5):632–642

Kurouski D, Van Duyne RP (2015) In situ detection and identification of hair dyes using surface-enhanced Raman spectroscopy (SERS). Anal Chem 87(5):2901–2906

Kurouski D, Lee H, Roschangar F, Senanayake Ch (2017) Surface-enhanced raman spectroscopy: from concept to practical application. Spectroscopy 32(11):36–44

Lakhani A, Malon P, Keiderling TA (2009) Comparison of vibrational circular dichroism instruments: development of a new dispersive VCD. Appl Spect 63(7):775–785

Larsen MR, Trelle MB, Thingholm TE, Jensen ON (2006) Analysis of posttranslational modifications of proteins by tandem mass spectrometry. Biotechniques 40(6):790–798

Leopold N, Lendl B (2003) A new method for fast preparation of highly surface-enhanced Raman scattering (SERS) active silver colloids at room temperature by reduction of silver nitrate with hydroxylamine hydrochloride. J Phys Chem B 107(24):5723–5727

Marenich AV, Cramer CJ, Truhlar DG (2009) Universal solvation model based on solute electron density and a continuum model of the solvent defined by the bulk dielectric constant and atomic surface tensions. J Phys Chem B 113(18):6378–6396

Martins VR, Beraldo FH, Hajj GN, Lopes MH, Lee KS, Linden PMAR (2010) Prion protein: orchestrating neurotrophic activities. Curr Issues Mol Biol 12(2):63–86

Martinsson E, Shahjamali MM, Large N, Zaraee N, Schatz GC, Aili D, Mirkin CA (2015) Influence of surfactant bilayers on the refractive index sensitivity and catalytic properties of anisotropic gold nanoparticles. Small 12(3):330–342

Meade RM, Fairlie DP, Mason JM (2019) Alpha-synuclein structure and Parkinson's disease—lessons and emerging principles. Mol Neurodegener 14:1

Mulfinger L, Solomon SD, Bahadory M, Jeyarajasingam AV, Rutkowsky SA, Boritz C (2007) Synthesis and study of silver nanoparticles. J Chem Educ 84(2):322–325

Mulvihill MJ, Ling XY, Henzie J, Yang P (2010) Anisotropic etching of silver nanoparticles for plasmonic structures capable of single-particle SERS. J Am Chem Soc 132(1):268–274

Niederhafner P, Šafařík M, Brichtová E, Šebestík J (2016) Rapid acidolysis of benzyl group as a suitable approach for synthesis of peptides naturally produced by oxidative stress and containing 3-nitrotyrosine. Amino Acids 48(4):1087–1098

Niederhafner P, Šafařík M, Brichtová E, Šebestík J (2019) Correction to: Rapid acidolysis of benzyl group as a suitable approach for syntheses of peptides naturally produced by oxidative stress and containing 3-nitrotyrosine. Amino Acids 51(10–12):1689–1690

Niederhafner P, Brichtová E, Šafařík M, Keiderling TA, Šebestík J (2019b) The role of tyrosine oxidation in structures and properties of neurodegenerative peptides and proteins. In Peptide Science 2018: Proceedings of the 10th International Peptide Symposium/The 55th Japanese Peptide Symposium. Shiroh Futaki and Katsumi Matsuzaki (Eds), The Japanese Peptide Society, Kyoto, pp 59–60

Novák V, Šebestík J, Bouř P (2012) Theoretical modeling of the surface-enhanced Raman optical activity. J Chem Theory Comput 8(5):1714–1720

Novák V, Dendisová M, Matějka P, Bouř P (2016) Explanation of surface-enhanced raman scattering intensities of p-aminobenzenethiol by density functional computations. J Phys Chem C 120(32):18275–18280

Oueslati A, Fournier M, Lashuel HA (2010) Role of post-translational modifications in modulating of structure, function and toxicity of alpha-synuclein. Implications for Parkinson's disease pathogenesis and therapies. Progress Brain Res 183(C):115–145

Perdew JP, Burke K, Wang Y (1996) Generalized gradient approximation for the exchange-correlation hole of a many-electron system. Phys Rev B 54(23):16533–16539

Pettersen EF, Goddard TD, Huang CC, Couch GS, Greenblatt DM, Meng EC, Ferrin TE (2004) UCSF Chimera: a visualization system for exploratory research and analysis. J Comput Chem 25(13):1605–1612

Quaroni L, Smith WE (1999a) Nitration of internal tyrosine of cytochrome *c* probed by resonance Raman scattering. Biospectroscopy 5:S71–S76

Quaroni L, Smith WE (1999b) The Nitro Stretch as a Probe of the Environment of Nitrophenols and Nitrotyrosines. J Raman Spectrosc 30(7):537–542

Radi R (2004) Nitric oxide, oxidants, and protein tyrosine nitration. Proc Natl Acad Sci USA 101(12):4003–4008

Radi R (2013) Protein tyrosine nitration: biochemical mechanisms and structural basis of functional effects. Acc Chem Res 46(2):550–559

Rahmelow K, Hübner W, Ackermann Th (1998) Infrared absorbances of protein side chains. Anal Biochem 257(1):1–11

Rehor I, Cigler P (2014) Precise estimation of HPHT nanodiamond size distribution based on transmission electron microscopy image analysis. Diam Relat Mater 46:21–24

Reynolds MR, Berry RW, Binder LI (2005) Site specific nitration and oxidative dityrosine bridging of the tau protein by peroxynitrite: implications for Alzheimer's disease. Biochemistry 44(5):1690–1700

Ruud K, Thorvaldsen AJ (2009) Theoretical approaches to the calculation of raman optical activity spectra. Chirality 21:E54–E67

Rycenga M, Langille MR, Personick ML, Ozel T, Mirkin CA (2012) Chemically isolating hot spots on concave nanocubes. Nano Lett 12(12):6218–6222

Rygula A, Majzner K, Marzec KM, Kaczor A, Pilarczyk M, Baranska M (2013) Raman spectroscopy of proteins: a review. J Raman Spectrosc 44(8):1061–1076

Seballos L, Richards N, Stevens DJ, Patel M, Kapitzky L, Lokey S, Millhauser G, Zhang JZ (2007) Competitive binding effects on surface-enhanced Raman scattering of peptide molecules. Chem Phys Lett 447(4–6):335–339

Šebestík J, Bouř P (2011) Raman optical activity of methyloxirane gas and liquid. J Phys Chem Lett 2(5):498–502

Šebestík J, Šafařík M, Bouř P (2012) Ferric complexes of 3-hydroxy-4-pyridinones characterized by density functional theory and Raman and UV-vis spectroscopies. Inorg Chem 51(8):4473–4481

Shao Z, Zhu W, Wang H, Yang Q, Yang S, Liu X, Wang G (2013) Controllable synthesis of concave nanocubes, right bipyramids, and 5-fold twinned nanorods of palladium and their enhanced electrocatalytic performance. J Phys Chem C 117(27):14289–14294

Sharma B, Frontiera RR, Henry AI, Ringe E, Van Duyne RP (2012) SERS: Material, applications and the future. Mater Today 15(1–2):16–25

Soum E, Brazzolotto X, Goussias C, Bouton C, Moulis J-M, Mattioli TA, Drapier J-C (2003) Peroxynitrite and nitric oxide differently target the iron-sulfur cluster and amino acid residues of human iron regulatory protein 1. Biochemistry 42(25):7648–7654

Stamplecoskie KG, Scaiano JC, Tiwari VS, Anis H (2011) Optimal size of silver nanoparticles for surface-enhanced raman spectroscopy. J Phys Chem C 115(5):1403–1409

Stiles PL, Dieringer JA, Shah NC, Van Duyne RP (2008) Surface-enhanced raman spectroscopy. Ann Rev Anal Chem 1(1):601–626

Stuart ChM, Frontiera RR, Mathies RA (2007) Excited-State structure and dynamics of cis- and *trans*-azobenzene from resonance Raman intensity analysis. J Phys Chem A 111(48):12072–12080

Sun M, Xu H (2012) A novel application of plasmonics: plasmon-driven surface-catalyzed reactions. Small 8(18):2777–2786

Taylor RW, Lee TC, Scherman OA, Esteban R, Aizpurua J, Huang FM, Baumberg JJ, Mahajan S (2011) Precise subnanometer plasmonic junctions for SERS within gold nanoparticle assemblies using cucurbit [n]uril "glue." ACS Nano 5(5):3878–3887

Tomasi J, Mennucci B, Cammi R (2005) Quantum mechanical continuum solvation models. Chem Rev 105:2999–3093

Tsikas D, Duncan MW (2014) Mass spectrometry and 3-nitrotyrosine: Strategies, controversies, and our current perspective. Mass Spectrom Rev 33(4):237–276

Tuma R (2005) Raman spectroscopy of proteins: from peptides to large assemblies. J Raman Spectrosc 36(4):307–319

Ulmer TS, Bax A, Cole NB, Nussbaum RL (2005) Structure and dynamics of micelle bound human alpha-synuclein. J Biol Chem 280:9595–9603

Valim LR, Davis JA, Jensen KT, Guo R, Willison KR, Spickett CM, Pitt AR, Klug DR (2014) Identification and relative quantification of tyrosine nitration in a model peptide using two-dimensional infrared spectroscopy. J Phys Chem B 118(45):12855–12864

Vana L, Kanaan NM, Hakala K, Weintraub ST, Binder LI (2011) Peroxynitrite-induced nitrative and oxidative modifications alter tau filament formation. Biochemistry 50(7):1203–1212

Venyaminov SYu, Kalnin NN (1990) Quantitative IR spectrophotometry of peptide compounds in water (H2O) Solutions. I. spectral parameters of amino acid residue absorption bands. Biopolymers 30(13–14):1243–1257

Woody AY, Woody RW (2003) Individual tyrosine side-chain contributions to circular dichroism of ribonuclease. Biopolymers 72(6):500–513

Yamamoto S, Bouř P (2013) Transition polarizability model of induced resonance Raman optical activity. J Comput Chem 34(25):2152–2158

Yamashiro D, Li CH (1973) Adrenocorticotropins 44 Total synthesis of the human hormone by the solid-phase method. J Am Chem Soc 95(4):1310–1315

Yanai T, Tew D, Handy N (2004) A new hybrid exchange-correlation functional using the Coulomb-attenuating method (CAM-B3LYP). Chem Phys Lett 393(1–3):51–57

Yttenberg AJ, Jensen ON (2010) Modification-specific proteomics in plant biology. J Proteomics 73(11):2249–2266

Zahn R, Liu A, Lührs T, Riek R, von Schroetter Ch, García FL, Billeter M, Calzolai L, Wider G, Wüthrich K (2000) NMR solution structure of the human prion protein. Proc Natl Acad Sci USA 97(1):145–150

Zhang Q, Large N, Nordlander P, Wang H (2014) Porous Au nanoparticles with tunable plasmon resonances and intense field enhancements for single-particle SERS. J Phys Chem Lett 5(2):370–374

Zhang Q, Large N, Wang H (2014) Gold nanoparticles with tipped surface structures as substrates for single-particle surface-enhanced Raman spectroscopy: concave nanocubes, nanotrisoctahedra, and nanostars. ACS Appl Mater Interf 6(19):17255–17267

Zhao Y, Truhlar DG (2008) The M06 suite of density functionals for main group thermochemistry, thermochemical kinetics, noncovalent interactions, excited states, and transition elements: two new functionals and systematic testing of four M06-class functionals and 12 other functionals. Theor Chem Acc 120(1–3):215–241

Zhao Y, Zhang Y, Sun H, Maroto R, Brasier AR (2017) Selective affinity enrichment of nitrotyrosine-containing peptides for quantitative analysis in complex samples. J Proteome Res 16(8):2983–2992

Zhao J, Wu J, Yang Z, Ouyang L, Zhu L, Gao Z, Hailing Li (2019) Nitration of hIAPP promotes its toxic oligomer formation and exacerbates its toxicity towards INS-1 cells. Nitric Oxide 87:23–30